ADVANCES IN ATMOSPHERIC SCIENCES, VOL. 37, MARCH 2020, 1–9

• Original Paper •

Comparison of Advanced Technology Microwave Sounder Biases Estimated Using Radio Occultation and Hurricane Florence (2018) captured by NOAA-20 and S-NPP

Xiaoxu TIAN and Xiaolei ZOU*

Earth Science System Interdisciplinary Center, University of Maryland

(Received 18 June 2019; revised 8 November 2019; accepted 19 November 2019)

ABSTRACT

The second Advanced Technology Microwave Sounder (ATMS) was onboard the National Oceanic and Atmospheric Administration (NOAA)-20 satellite when launched on 18 November 2017. Using nearly six months of the earliest NOAA-20 observations, the biases of the ATMS instrument were compared between NOAA-20 and the Suomi National Polar-Orbiting Partnership (S-NPP) satellite. The biases of ATMS channels 8 to 13 were estimated from the differences between antenna temperature observations and model simulations generated from Meteorological Operational (MetOp)-A and MetOp-B satellites' Global Positioning System (GPS) radio occultation (RO) temperature and water vapor profiles. It was found that the ATMS onboard the NOAA-20 satellite has generally larger cold biases in the brightness temperature measurements at channels 8 to 13 and small standard deviations. The observations from ATMS on both S-NPP and NOAA-20 are shown to demonstrate an ability to capture a less than 1-h temporal evolution of Hurricane Florence (2018) due to the fact that the S-NPP orbits closely follow those of NOAA-20.

Key words: ATMS, NOAA-20, S-NPP, biases, Hurricane Florence

Citation: Tian, X. X, and X. L. Zou, 2020: Comparison of Advanced Technology Microwave Sounder biases estimated using radio occultation and Hurricane Florence (2018) captured by NOAA-20 and S-NPP. *Adv. Atmos. Sci.*, **37**(3), https://doi.org/10.1007/s00376-019-9119-5. (in press)

Article Highlights:

- Biases of ATMS onboard NOAA-20 were characterized by comparing observations with CRTM simulations with GPS RO profiles.
- Results showed that NOAA-20 ATMS observations are more negatively biased than those from the S-NPP ATMS.
- The 50-min-apart orbiting setup of NOAA-20 and S-NPP enables a better temporal resolvability of Hurricane Florence.

1. Introduction

The National Oceanic and Atmospheric Administration (NOAA)-20 satellite, designated Joint Polar Satellite System-1 before launch, was successfully launched into a sun-synchronous orbit on 18 November 2017. The equator crossing time (ECT) of NOAA-20 is around 1330 local time for the ascending node, which covers the majority of the Earth twice daily. NOAA-20 carries the second Advanced Technology Microwave Sounder (ATMS). The first ATMS was onboard the Suomi National Polar-orbiting Partnership (S-NPP) satellite, launched on 28 October 2011, also with an ECT of 1330 local time. While the ECTs of NOAA-20 and S-NPP are the same, the reference points on the equator of 1330 local time are different. ATMS is a cross-track microwave radiometer that observes radiances at a total of 22 channels for atmospheric temperature and moisture profiling with a spatial resolution of about 32 km for temperature sounding channels at nadir. The detailed channel features for the S-NPP ATMS, such as center frequencies, specifications, on-orbit noise equivalent delta temperature (NEDT), and so on, are listed in Table 1 (ATBD, 2013; Kim et al., 2014; Zou et al., 2014; Zou and Tian, 2018). The ATMS onboard NOAA-20 has exactly the same channel settings as the S-NPP ATMS but with substantially updated hardware, the impact of which is quantified in this study and discussed in later sections. The first set of NOAA-20 ATMS observational data was transmitted back to Earth on 29 November 2017.

Spaceborne microwave remote sensing observations, such as ATMS, are a key data type for numerical weather prediction (NWP). Zou et al. (2013) demonstrated that the assimilation of ATMS radiances into the Hurricane Weather Re-

* Corresponding author: Xiaolei ZOU
Email: xzou1@umd.edu

search and Forecasting model helps to improve both the hurricane track and intensity forecast performance. Previous studies have also shown positive impacts on global weather forecast skill brought by the Advanced Microwave Sounding Unit-A (AMSU-A), which is the predecessor of ATMS (Eyre et al., 1993; Andersson et al., 1994; Derber and Wu, 1998; Qin et al., 2012). Besides being a part of observational inputs for NWP models, their applications also include retrieving surface temperatures, atmospheric temperatures, total precipitable water, liquid water paths, and ice water paths under almost all weather conditions except for heavy precipitation. Tian and Zou (2016) showed that the measurements from both AMSU-A and ATMS can be used to analyze the three-dimensional hurricane warm-core structures with a temperature profile retrieval algorithm they proposed. Tian and Zou (2018) combined the microwave temperature sounder instruments on multiple satellites to retrieve the three-dimensional warm-core structure temporal evolutions in Hurricanes Harvey, Irma, and Maria. Zou and Tian (2018) further refined the temperature retrieval algorithm by training the retrieval coefficients with Global Positions System (GPS) radio occultation (RO) temperature profiles for achieving better accuracies of the temperature retrieval products.

However, before any of these applications, the bias features of each channel have to be characterized. Any bias has to be properly quantified and then removed. Zou et al. (2014) characterized the noise and bias characteristics of the ATMS onboard S-NPP using NWP analysis/forecast fields. ATMS brightness temperatures (TBs) were simulated with atmospheric temperature and water vapor profiles from GPS RO observations as an input to the Community Radiative Transfer Model (CRTM). CRTM is known to be able to rapidly simulate radiances with an accuracy of less than 0.1 K for microwave sensors (Liu et al., 2013). It was shown that S-NPP ATMS biases for the temperature sounding channels 5–15 could be well characterized by GPS RO data. In this study, the in-orbit accuracy of the ATMS onboard both the recently launched NOAA-20 satellite and the S-NPP satellite were estimated using GPS RO level-2 retrieval profiles from the two Global Navigation Satellite System (GNSS) Receivers for Atmospheric Sounding (GRAS) onboard the Meteorological Operational (MetOp)-A and MetOp-B satellites (Gorbunov et al., 2011).

Since NOAA-20 operates in the same orbit as S-NPP but about 50 min ahead of it, NOAA-20 allows an important overlap in ATMS observational coverage. This gives meteorologists a new opportunity to obtain ATMS information at a half-hour interval, twice daily, for fast-evolving weather systems such as hurricanes. An example is shown in this regard for Hurricane Florence (2018).

2. GPS RO data for post-launch calibration of ATMS biases

2.1. *Data description*

Atmospheric temperature and humidity profiles retrieved from GPS RO observations of the GRAS instrument onboard both MetOp-A and -B serve as inputs for model simulations of ATMS antenna temperatures. With the aid of the Radio Occultation Processing Package, the raw RO measurements of excess Doppler shifts can be used to retrieve the atmospheric refractivity. The GPS RO level-2 atmospheric temperature and humidity profiles can then be retrieved from the refractivity with a one-dimensional variational data assimilation method with the 137-level ECMWF reanalysis data as first guess (Healy and Eyre, 2000; Culverwell et al., 2015). The horizontal resolution of each RO profile is about 270 km (Kursinski et al., 1997). The estimated errors for temperature profiles are less than 1 K from the surface to about 40 km and less than 0.4 K for the layer from 8 km to 25 km (Angling, 2016). The GPS RO level-2 retrieval profiles used in this study were provided by the Radio Occultation Meteorology Satellite Application Facility (ROM SAF) under the European Organisation for the Exploitation of Meteorological Satellites (EUMETSAT) (Nielsen et al., 2016). The MetOp-A and -B RO mission can generate approximately 1200 level-2 temperature/humidity profiles daily. In order to estimate the biases in ATMS measurements of antenna temperatures, the observed ATMS antenna temperatures (temperature data records) during the period from 23 January to 23 July 2018 were compared against the CRTM-simulated TBs generated with RO profile data during the same time period as input background information to the CRTM.

2.1. *Methodology*

In practice, before any TB simulations, a bi-weight quality control (QC) needs to first be applied to the MetOp-A and -B RO profile data to ensure the validity and quality of RO profiles input into CRTM. The first step in the QC procedures is to ensure all refractivity values are physical, i.e., positive. The bi-weight mean and bi-weight standard deviations of the temperatures at different pressure levels are then calculated. In order to ensure that all RO profiles input into CRTM are of reasonable accuracy, outliers whose deviations from the bi-weight mean are 2.5 times larger than the bi-weight standard deviation are further excluded. More details regarding the formulation and the bi-weight QC method can be found in Zou and Zeng (2006).

RO profiles that pass the abovementioned bi-weight QC procedures are collocated with ATMS observations from both S-NPP and NOAA-20 under the criteria of being within a 100-km spatial distance and 3-h time difference (Zou et al., 2014). The total numbers of GRAS RO profiles collocated within ATMS observations from S-NPP and NOAA-20 are 34 965 and 35 870 under clear-sky conditions, respectively, and 48 743 and 46 964 under cloudy conditions, respectively. Above 800 hPa, less than 10% of data are masked out by the bi-weight QC (Fig. 1). All of these collocated RO profiles are then used as inputs to the CRTM to generate ATMS simulations.

3. Comparison of ATMS biases between S-NPP and NOAA-20

The differences between observed and simulated an-

tenna temperatures (i.e., O-B) over the time period from 23 January to 23 July 2018 were analyzed to characterize the bias features of channels 8 to 13. The levels of peak weighting functions at channel 8 and 13 are given in Fig. 1, indicating the layers of the atmosphere that channels 8–13 are mainly sensitive to. ATMS channels 5–7 are not included in this study since these lower-level channels could be strongly affected by clouds (Zou and Tian, 2018, 2019) and GPS RO profiles in the lower troposphere could be affected by multiple pathways (Zou et al., 2019). Figure 2 gives the mean and standard deviation values of the nadir O-B data sample for the ATMS onboard NOAA-20 and S-NPP with and without the bi-weight QC for the selection of RO profiles. The ATMS antenna temperature observations from NOAA-20 (blue bars) are more negatively biased than those of the S-NPP ATMS antenna temperature observations (black bars) (Fig. 2a). The differences in bias introduced by the QC procedures are minor for channels 8–11 of both ATMS instruments. Figure 2b shows the standard deviations of O-B. The standard deviations of the NOAA-20 ATMS are generally smaller than those of the S-NPP ATMS antenna temperatures. This implies that the observational performance of the NOAA-20 ATMS is better in terms of precision than those of S-NPP when compared to simulated TBs. Comparing the standard deviation results before and after the QC, the QC procedures removing the outliers in RO profiles reduce the standard deviations in O-B as expected. The red curve in Fig. 2b represents the specifications of S-NPP ATMS at channels 8–13. The standard deviations are below the specification values for channels 8–9 and 11–13, implying that observation errors are much smaller than the specifications. For channel 10, the standard deviation for S-NPP ATMS is slightly larger than the specification, which could come from a contribution of increased GPS RO retrieval errors at high altitudes (~25 km and above) (Kuo et al., 2004). Despite similar NEDT at each channel, the standard deviations increase with channel numbers, i.e., increasing height of the corresponding peak weighting functions, with the exception of channel 10.

Figure 3 shows scatterplots of S-NPP and NOAA-20 ATMS O-B values at channel 9 versus those at channel 8. The distribution of the NOAA-20 (Fig. 3b) data points looks tighter than that of the S-NPP (Fig. 3a) data points, which is also reflected by a smaller standard deviation of the former than the latter. Figure 3 also shows the minimal impacts of clouds on these upper-level channels and the small differences of the bias and standard deviation between all-weather and clear-sky-only data. An inter-channel correlation of O-B between channels 8 and 9 is seen for NOAA-20 and S-NPP.

The ATMS is a cross-track scanning radiometer, meaning the optical path varies with scan angle. Figure 4a shows the number of RO profiles collocated with ATMS observation pixels at each field of view (FOV) position from 23 Janu-

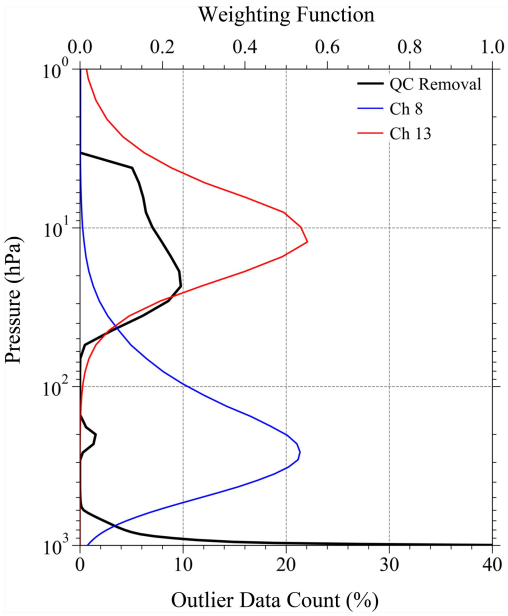

Fig. 1. Variations of data count removed in the bi-weight QC with respect to pressure (black curve) and the weight functions of channels 8 (blue curve) and 13 (red curve).

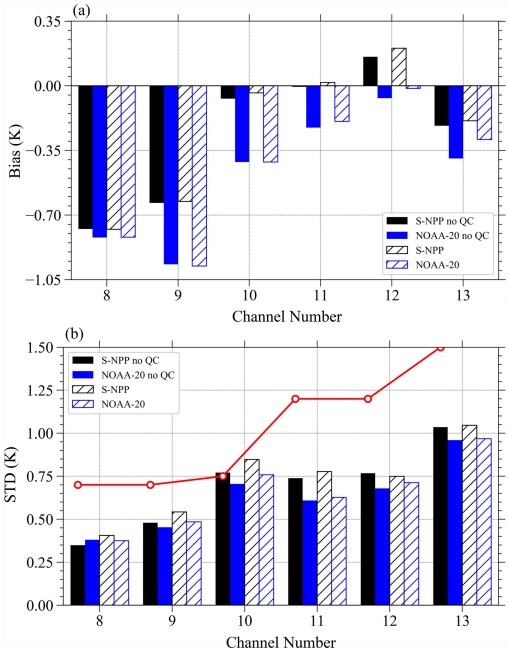

Fig. 2. (a) Biases and (b) standard deviations of ATMS channels 8–13 calculated from the differences in TBs between the S-NPP (black bars) and NOAA-20 (blue bars) observations and RO/CRTM simulations at nadir FOVs during the 6-month period from 23 January to 23 July 2018. The red curve indicates the specification values of S-NPP ATMS channels.

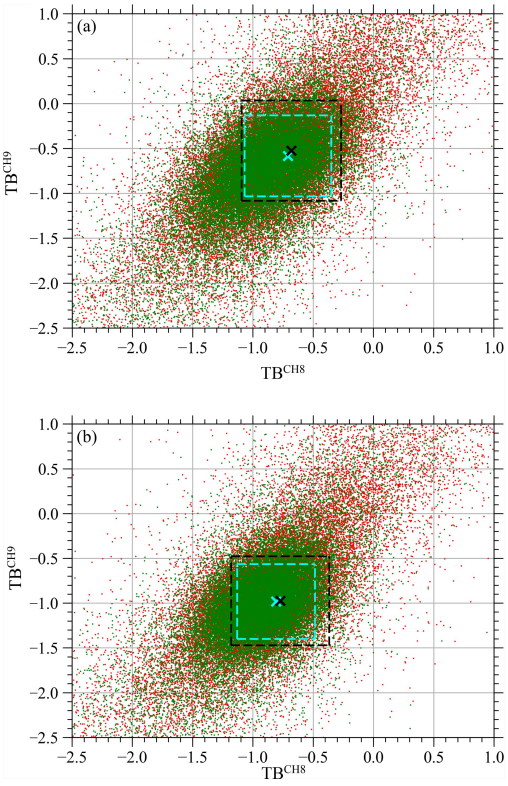

Fig. 3. Differences in the observed and simulated TB (K), i.e. O-B, of channel 9 with respect to channel 8 for the ATMS onboard (a) S-NPP and (b) NOAA-20 under clear-sky (green dots) and cloudy (red dots) conditions. The mean values of clear-sky (cyan) and cloudy (black) conditions are indicated by the black cross, and standard deviations by the dashed box. Only nadir observations were included when calculating the mean and standard deviation values.

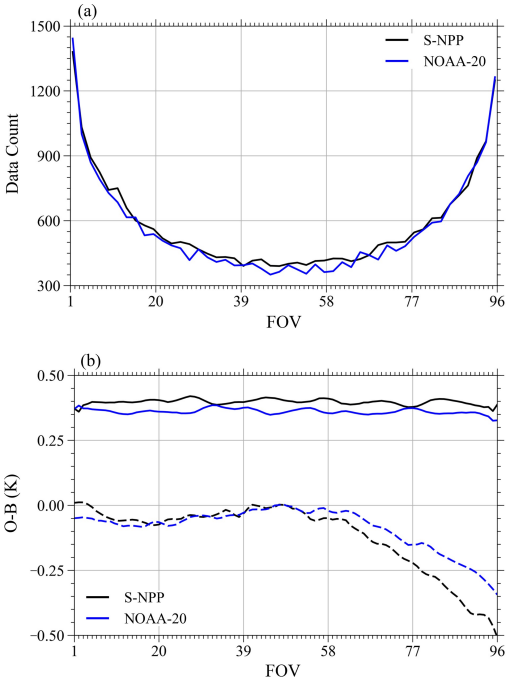

Fig. 4. (a) Data count and (b) biases (dashed curves) with standard deviations (solid curves) of channel 8 of ATMS onboard S-NPP (black) and NOAA-20 (blue) calculated with simulated TBs with RO as backgrounds from 23 January to 23 July 2018. Profiles under all-sky conditions were included in the calculations.

ary to 23 July 2018. The FOV denotes the angle of view at which the ATMS can effectively detect the radiation. About 600 RO profiles are collocated near nadir ATMS FOVs. The numbers of collocated GRAS RO profiles rapidly increase at larger scan-angle positions, resulting from larger FOV sizes and larger spatial separations between the centers of two neighboring FOVs at larger scan angles. Figure 4b shows the means (dashed) and standard deviations (solid) of the O-B of channel 8 at the 96 scan positions for the ATMS onboard NOAA-20 (blue) and S-NPP (black). The ATMS scan biases, with the biases calculated at nadir subtracted, are asymmetric with respect to scan angle for both NOAA-20 and S-NPP, with much smaller scan variation on the side of FOVs 1–48 than the side of FOVs 49–96. This asymmetry was found to be caused by the antenna sidelobe intercepts with the spacecraft, as ATMS is mounted on the side of the spacecrafts (Kim et al., 2014). It is also apparent that the NOAA-20 ATMS scan biases are smaller in magnitude than those of S-NPP on the side of FOVs 49–96. The standard deviations for both ATMS instruments show no significant scan-dependent features. Similar to the results in Fig. 2b, the NOAA-20 ATMS standard deviations are generally smaller than those of the S-NPP ATMS at most FOV positions. Figure 5 shows the O-B biases at channels 8–13 as functions of the 96 scan angles for the ATMS onboard NOAA-20 and S-NPP. Similar to channel 8 (Fig. 4b), the scan-dependent biases at channels 9–13 for the NOAA-20 ATMS are generally smaller than those for the S-NPP ATMS (Fig. 5). The patterns for NOAA-20 ATMS channels 12 and 13 appear less symmetric than those for the corresponding S-NPP ATMS channels. Scan biases for channels 9–11 display similar asymmetries with respect to FOV positions as that of channel 8.

Previous studies, including Zou et al. (2014) and Weng et al. (2013), have reported latitudinal dependences of microwave temperature sounder data biases. The latitudinal features of the NOAA-20 ATMS were examined by grouping the RO profiles collocated with ATMS near nadir pixels in every 10° latitudinal band. Figure 6a shows the data counts of RO profiles collocated with ATMS observations at nadir (FOV positions 47 and 48) within each latitudinal band. Figure 6b shows the means (dashed) and standard deviations (solid) of O-B at channel 8 as functions of latitudinal bands for

the ATMS onboard NOAA-20 and S-NPP. Consistent with previous results, the NOAA-20 ATMS biases are greater in both magnitude and latitudinal variation than those of the S-NPP ATMS. The NOAA-20 ATMS biases are largest at high latitudes. The standard deviations show a similar pattern, with larger magnitudes at higher latitudes. Figure 7 shows the latitudinal bias distributions for ATMS channels 8–13. There is a strong latitudinal dependence of the ATMS biases from both S-NPP (Fig. 7a) and NOAA-20 (Fig. 7b). These latitudinal dependences are possibly due to the opposite sign of O-B in the background, i.e., RO profiles (Wang and Zou, 2012). The magnitudes of the biases of channels 8 and 9 are greater at low latitudes than at high latitudes, and vice versa for channels 10–13. Since S-NPP and NOAA-20 ATMSs use the same radiance-based calibration algorithm, the ATMS bias differences between S-NPP and NOAA-20 could arise from some coefficients in the processing coefficient tables, which are sensor-dependent and different for these two satellites (Ninghai SUN, personal communication, 2018?).

As the NOAA-20 ATMS has larger negative biases and smaller standard deviations than those of the S-NPP ATMS, the updated bias correction and error variance estimation for the NOAA-20 ATMS is required in order to assimilate NOAA-20 ATMS data in NWP and in linking ATMS observations from NOAA-20 to those of S-NPP and AMSU-A for climate studies.

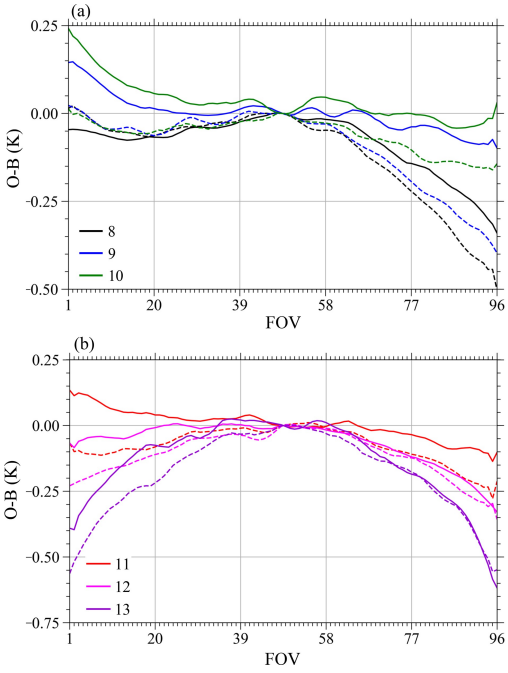

Fig. 5. Biases of channels (a) 8–10 and (b) 11–13 of the ATMS onboard NOAA-20 (solid curves) and S-NPP (dashed curves) with respect to scan positions under all-sky conditions.

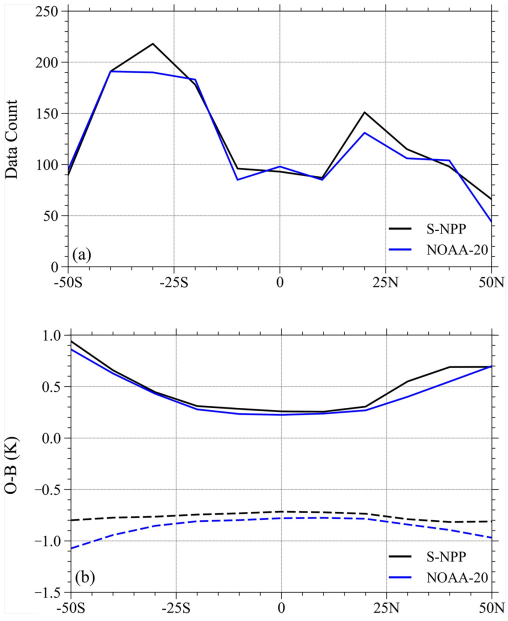

Fig. 6. (a) Data count and (b) the mean (dashed curves) and standard deviations (solid curves) of O-B with respect to latitudinal bands of every 10° for the ATMS onboard S-NPP (black) and NOAA-20 (blue) for observations from 23 January to 23 July 2018. Profiles under all-sky conditions were included in the calculations.

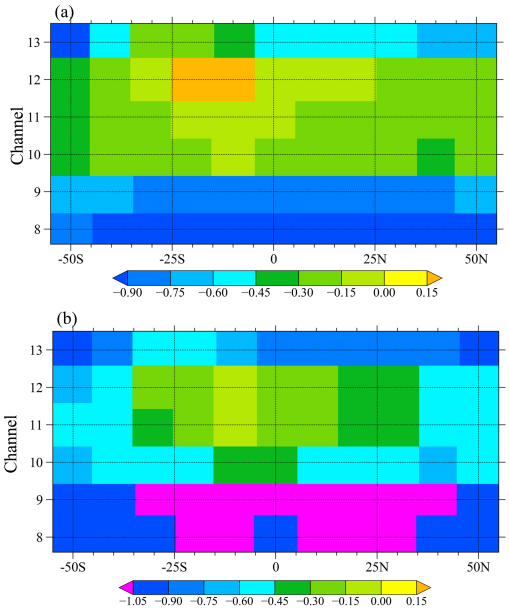

Fig. 7. The mean differences of O-B at channels 8–13 with respect to latitudinal bands at every 10° calculated from 23 January to 23 July 2018 for the ATMS onboard (a) S-NPP and (b) NOAA-20. Profiles under all-sky conditions were included in the calculations.

4. NOAA ATMS in Hurricane Florence

Hurricane Florence was the first major hurricane in 2018 over the Atlantic Ocean. Originated from a tropical wave off the west coast of Africa, Florence acquired the intensity of a Category 4 Hurricane after an explosive intensification on 5 September, and weakened to a tropical storm before 7 September 2018. It then re-intensified to a Category 4 hurricane on 10 September and posed serious threats to the east coast of the United States. The ATMS TB observations from both NOAA-20 and S-NPP during the lifespan of Hurricane Florence were used to demonstrate the measuring capability of the 50-min back-to-back orbiting arrangement. Figure 8 shows the TBs at ATMS channels 6 and 8 from S-NPP at 1629 UTC (Fig. 8a) and NOAA-20 at 1718 UTC (Fig. 8b) 10 September 2018. The intensity of Hurricane Florence had just reached Category 4 around this time. When the S-NPP ATMS was scanning through the storm, the hurricane center happened to be covered near the edge of a S-NPP ATMS swath. After only 49 min, the NOAA-20 ATMS was able to measure radiances surrounding Hurricane Florence again. At this time, the storm center was located in the middle of an ATMS swath, i.e., the nadir position of NOAA-20.

ATMS, as mentioned in section 1, is a cross-track scanning radiometer with constantly changing scan angles in one scan line. The TB measurements thus have scan dependence, or limb effects, that can conceal much of the hur-

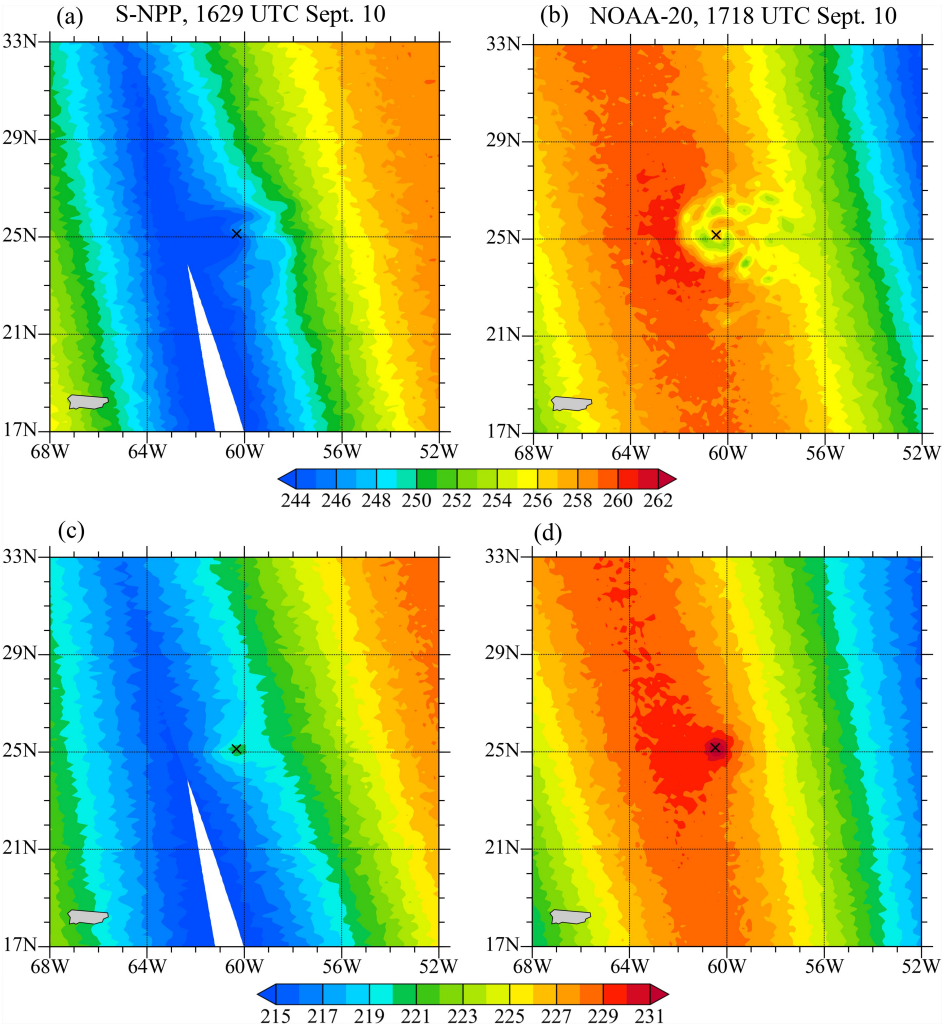

Fig. 8. TB (K) observations at ATMS (a, b) channel 6 and (c, d) channel 8 from (a, c) S-NPP ATMS at 1629 UTC and (b, d) NOAA-20 ATMS at 1718 UTC on 10 September 2018 within and around Hurricane Florence. The hurricane center from the best-track data are indicated by a black cross symbol.

ricane's features. These limb effects can be removed by using the method described and applied in Zou and Tian (2018) and Tian et al. (2018). One may also use it to remove the prevailing scan variations to reveal the storm structures hidden in the TB measurements. NOAA-20 ATMS observations from 1 to 31 August 2018 were used to train the coefficients of limb correction. Figure 9 shows the mean scan variations in the TBs of ATMS channels 5–12 onboard S-NPP (solid) and NOAA-20 (dashed) as well as their differences (dotted). The scan patterns of the two ATMS instruments generally agree well with each other; both have some minor asymmetric distributions. The limb-corrected TB observations are given in Fig. 10. The storm's rain-band features, which are vaguely visible in Fig. 8, can be clearly seen in the limb-corrected TB observations from both NOAA-20 and S-NPP, regardless of the storm's relative location within a swath. Although Hurricane Florence was observed near the edge of an S-NPP ATMS swath, the warm center and cold rain bands (Figs. 10a and c) are as successfully recovered as those located near the nadir of a NOAA-20 ATMS swath (Figs. 10b and d) by the limb correction. In this instance, the center of Hurricane Florence was covered by NOAA-20 ATMS 50 min after the S-NPP ATMS; the limb-corrected ATMS measurements also enable the capture of the evolutions of the warm center during the 50 min.

5. Summary and conclusions

The NOAA-20 satellite was successfully launched into a sun-synchronous orbit that is 50 min, or half an orbit, ahead of the orbit of the S-NPP satellite. This orbiting arrangement ensures a considerable amount of overlapping observational coverage when both satellites are operational. As both satellites carry the same set of meteorological instruments, the arrangement also guarantees the continuity of observations if S-NPP becomes deactivated in the future. ATMS is a microwave temperature and humidity sounder carried by both satellites. The biases of three upper-tropospheric and three lower-stratospheric temperature-sounding channels, i.e., channels 8–13, of ATMS onboard NOAA-20 satellite were characterized in this study by comparing observations with CRTM simulations during a six-month period from the first day when ATMS data reached beta maturity (23 January 2018) to 23 July 2018. MetOp-A and -B GPS RO profiles provided by the EUMETSAT ROM-SAF served as inputs to the radiative transfer model. More than 63 000 RO profiles from MetOp-A and MetOp-B were collocated with ATMS observations from the S-NPP and NOAA-20 satellites under the criteria of being within a 100-km distance and 3-h time difference. The comparison between the NOAA-20 and S-NPP ATMS channel 8–13 biases shows that NOAA-20 ATMS antenna temperature observations are

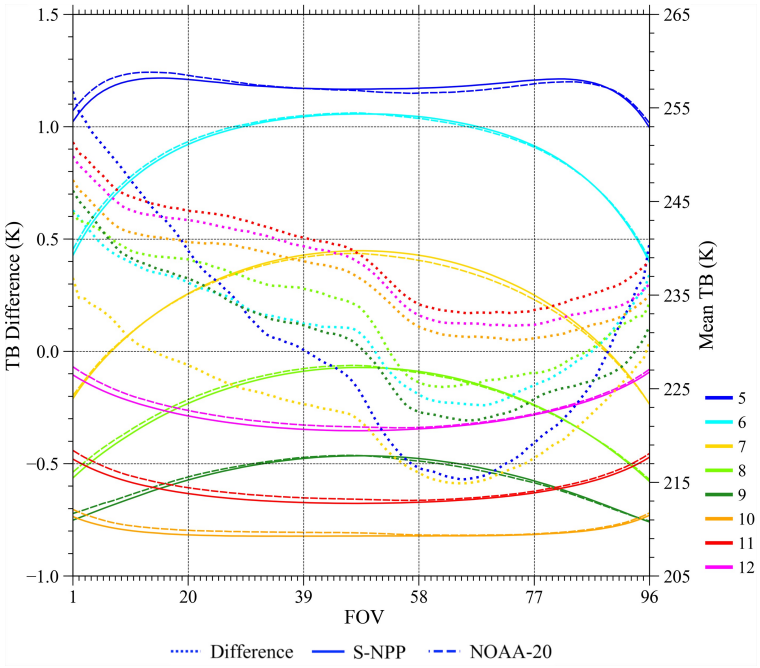

Fig. 9. Scan variations in global mean TBs of ATMS channels 5–12 (solid lines for S-NPP and dashed lines for NOAA-20) and differences in mean TBs between NOAA-20 and S-NPP (dotted lines). Results shown in all panels were calculated using data from January and August 2018.

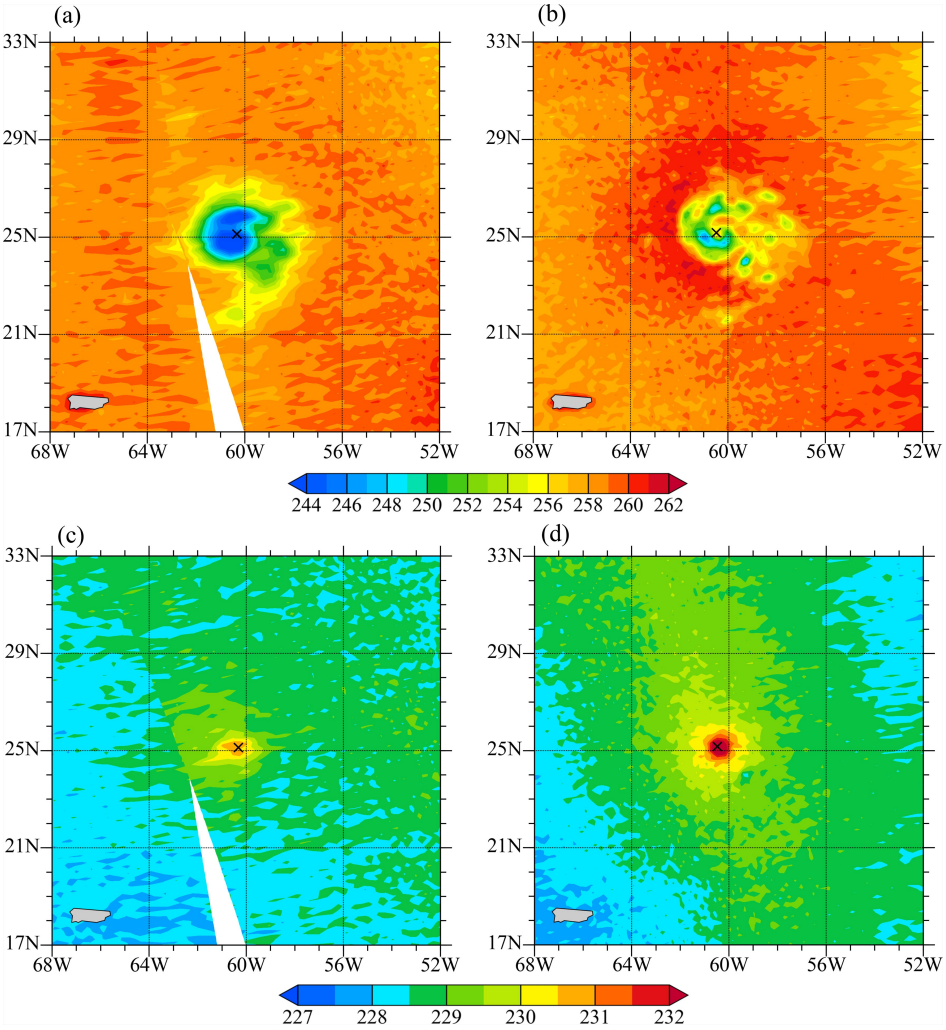

Fig. 10. TBs (K) after limb corrections at (a, b) channel 6 and (c, d) channel 8 observed by (a, c) S-NPP ATMS at 1629 UTC and (b, d) NOAA-20 ATMS at 1718 UTC on 10 September 2018 within and around Hurricane Florence. The center of Hurricane Florence from the best-track data is indicated by a black cross symbol. References.

more negatively biased than those from the S-NPP ATMS. It was also found that the NOAA-20 ATMS has been operating more stably, as indicated by smaller standard deviations in the O-B during the six-month observation period. The scan-varying latitudinal dependences of the NOAA-20 and S-NPP ATMS biases are generally similar.

The observations of ATMS onboard both satellites in the case of Hurricane Florence (2018) were examined in this study. It was found that the hurricane can be covered by ATMS measurements that are 50 min apart from both satellites, giving up to four ATMS coverages daily. This back-to-back orbiting setup enables a better temporal resolvability with cloud penetrating microwave observations over extreme weather events like Hurricane Florence. The limb-effect correction algorithm was applied to ATMS antenna temperature observations to reveal the structures of Hurricane Florence embedded but not visible in the antenna temperature observations. Future studies should include better quantitative comparisons of NOAA-20 ATMS instrument biases and other features, such as seasonal and annual variations, with ATMS and AMSU-A instrument biases.

Acknowledgements. This research was supported by NOAA (Grant No. NA14NES4320003). The authors are grateful to those who contributed to the Comprehensive Large Array-data Stewardship System for providing the ATMS observation data, and to ROM SAF for providing the RO profile data. The software developed to perform the calculations in this study is available by con-

tacting the Corresponding Author, Xiaolei ZOU, at xzou1@umd.edu.

REFERENCES

Andersson, E., J. Pailleux, J.-N. Thépaut, J. R. Eyre, A. P. McNally, G. A. Kelly, and P. Courtier, 1994: Use of cloud ‐ cleared radiances in three/four ‐ dimensional variational data assimilation. *Quart. J. Roy. Meteorol. Soc.*, **120**, 627–653, https://doi.org/10.1002/qj.49712051707.

Angling, M., 2016: ROM SAF CDOP-2 visiting scientist report 28: A new software tool for reducing systematic residual ionospheric errors in GNSS-RO level 3 products, SAF/ROM/DMI/REP/VS/28.

ATBD, J. A., 2013: Joint Polar Satellite System (JPSS) Advanced Technology Microwave Sounder (ATMS) SDR Calibration Algorithm Theoretical Basis Document (ATBD), JPSS ATBD #1.

Culverwell, I. D., H. W. Lewis, D. Offiler, C. Marquardt, and C. P. Burrows, 2015: The Radio Occultation Processing Package, ROPP. *Atmospheric Measurement Techniques*, **8**, 1887–1899, https://doi.org/10.5194/amt-8-1887-2015.

Derber, J. C., and W.-S. Wu, 1998: The use of TOVS cloud-cleared radiances in the NCEP SSI analysis system. *Mon. Wea. Rev.*, **126**, 2287–2299, https://doi.org/10.1175/1520-0493(1998)126<2287:TUOTCC>2.0.CO;2.

Eyre, J. R., G. A. Kelly, A. P. McNally, E. Andersson, and A. Persson, 1993: Assimilation of TOVS radiance information through one ‐ dimensional variational analysis. *Quart. J. Roy. Meteorol. Soc.*, **119**, 1427–1463, https://doi.org/10.1002/qj.49711951411.

Gorbunov, M. E., K. B. Lauritsen, H.-H. Benzon, G. B. Larsen, S. Syndergaard, and M. B. Sørensen, 2011: Processing of GRAS/METOP radio occultation data recorded in closed-loop and raw-sampling modes. *Atmospheric Measurement Techniques*, **4**, 1021–1026, https://doi.org/10.5194/amt-4-1021-2011.

Healy, S. B., and J. R. Eyre, 2000: Retrieving temperature, water vapour and surface pressure information from refractive ‐ index profiles derived by radio occultation: A simulation study. *Quart. J. Roy. Meteorol. Soc.*, **126**, 1661–1683, https://doi.org/10.1002/qj.49712656606.

Kim, E., C. H. J. Lyu, K. Anderson, R. Vincent Leslie, and W. J. Blackwell, 2014: S ‐ NPP ATMS instrument prelaunch and on ‐ orbit performance evaluation. *J. Geophys. Res.*, **119**, 5653–5670, https://doi.org/10.1002/2013JD020483.

Kuo, Y.-H., T.-K. Wee, S. Sokolovskiy, C. Rocken, W. Schreiner, D. Hunt, and R. A. Anthes, 2004: Inversion and error estimation of GPS radio occultation data. *J. Meteorol. Soc. Japan*, **82**, 507–531, https://doi.org/10.2151/jmsj.2004.507.

Kursinski, E. R., G. A. Hajj, J. T. Schofield, R. P. Linfield, and K. R. Hardy, 1997: Observing Earth's atmosphere with radio occultation measurements using the Global Positioning System. *J. Geophys. Res.*, **102**, 23429–23465, https://doi.org/10.1029/97JD01569.

Liu, Q. H., Y. Xue, and C. Li, 2013: Sensor-based clear and cloud radiance calculations in the community radiative transfer model. *Appl. Opt.*, **52**, 4981–4990, https://doi.org/10.1364/AO.52.004981.

Nielsen, J. K., S. Syndergaard, and K. B. Lauritsen, 2016: NRT Level 2b and 2c 1D-Var products (Metop-A: GRM-02, 03, 04, 05) (Metop-B: GRM-41, 42, 43, 44). ROM SAF CDOP-2.

Qin, Z., X. Zou, and F. Weng, 2012: Comparison between linear and nonlinear trends in NOAA-15 AMSU-A brightness temperatures during 1998-2010. *Climate Dyn.*, **39**, 1763–1779, https://doi.org/10.1007/s00382-012-1296-1.

Tian, X. X., and X. L. Zou, 2016: ATMS- and AMSU-A-derived hurricane warm core structures using a modified retrieval algorithm. *J. Geophys. Res.*, **121**, 12630–12646, https://doi.org/10.1002/2016JD025042.

Tian, X. X., and X. L. Zou, 2018: Capturing size and intensity changes of hurricanes irma and maria (2017) from polar-orbiting satellite microwave radiometers. *J. Atmos. Sci.*, **75**, 2509–2522, https://doi.org/10.1175/JAS-D-17-0315.1.

Tian, X. X., X. L. Zou, and S. P. Yang, 2018: A limb correction method for the microwave temperature sounder 2 and its applications. *Adv. Atmos. Sci.*, **35**, 1547–1552, https://doi.org/10.1007/s00376-018-8092-8.

Wang, X., and X. L. Zou, 2012: Quality assessments of Chinese FengYun-3B microwave temperature sounder (MWTS) measurements. *IEEE Trans. Geosci. Remote Sens.*, **50**, 4875–4884, https://doi.org/10.1109/TGRS.2012.2196438.

Weng, F. Z., and Coauthors, 2013: Calibration of Suomi national polar-orbiting partnership advanced technology microwave sounder. *J. Geophys. Res.*, **118**, 11187–11200, https://doi.org/10.1002/jgrd.50840.

Zou, X., and Z. Zeng, 2006: A quality control procedure for GPS radio occultation data. *J. Geophys. Res.*, **111**, D02112, https://doi.org/10.1029/2005JD005846.

Zou, X. L., and X. X. Tian, 2018: Hurricane warm-core retrievals from AMSU-a and remapped atms measurements with rain contamination eliminated. *J. Geophys. Res.*, **123**, 10815–10829, https://doi.org/10.1029/2018JD028934.

Zou, X. L., H. Liu, and Y. H. Kuo, 2019: Occurrence and detection of impact multipath simulations of bending angle. *Quart. J. Roy. Meteorol. Soc.*, **721**, 1690–1704, https://doi.org/10.1002/qj.3520.

Zou, X. L., and X. X. Tian, 2019: Comparison of ATMS striping noise between NOAA-20 and S-NPP and noise impact on warm core retrieval of typhoon jelawat (2018). *IEEE Journal of Selected Topics in Applied Earth Observations and Remote Sensing*, **12**, 2504–2512, https://doi.org/10.1109/JSTARS.2019.2891683.

Zou, X., F. Weng, B. Zhang, L. Lin, Z. Qin, and V. Tallapragada, 2013: Impacts of assimilation of ATMS data in HWRF on track and intensity forecasts of 2012 four landfall hurricanes. *J. Geophys. Res.*, **118**, 11558–11576, https://doi.org/10.1002/2013JD020405.

Zou, X. L., L. Lin, and F. Z. Weng, 2014: Absolute calibration of ATMS upper level temperature sounding channels using GPS RO observations. *IEEE Trans. Geosci. Remote Sens.*, **52**, 1397–1406, https://doi.org/10.1109/TGRS.2013.2250981.